Planetary ENA imaging: Effects of different interaction models for Mars

H. Gunell [a,*], M. Holmström [a], S. Barabash [a], E. Kallio [b], P. Janhunen [b], A. F. Nagy [c], and Y. Ma [c]

[a] *Swedish Institute of Space Physics, Box 812, SE-981 28 Kiruna, Sweden*

[b] *Finnish Meteorological Institute, Helsinki, Finland*

[c] *Space Physics Research Laboratory, Department of Atmospheric, Oceanic, and Space Sciences, University of Michigan, Ann Arbor, Michigan, USA*

Abstract

We present and compare energetic neutral atom (ENA) images that are calculated from plasma parameters given by three different simulation models of the interaction between the solar wind and Mars. The images are calculated by combining a model for the ion flow with a model of the neutral atmosphere using the cross sections for the charge exchange collisions. The three ion models are: an empirical model that is based on Phobos 2 measurements; a three-dimensional hybrid simulation; and a three-dimensional MHD simulation. For the empirical and MHD models the images are obtained by integration of the ENA emission along lines of sight to a virtual ENA instrument. In the case of the hybrid model images are obtained by summing the contributions from all ions, whose positions, velocities, and weights are saved in files at regular intervals.

Differences between the models can be detected in the images, for example the hybrid model produces ENA emissions from a larger region than the MHD model does. An asymmetry in the oxygen ion density develops in the hybrid model and can be seen in the oxygen ENA images. The images are influenced by finite gyro radius effects, which are included in the hybrid model but not in the other two. The total production rates of hydrogen ENAs are $2.7 \cdot 10^{25}\mathrm{s}^{-1}$, $5.8 \cdot 10^{25}\mathrm{s}^{-1}$, and $2.4 \cdot 10^{25}\mathrm{s}^{-1}$ for the empirical, hybrid and MHD models respectively.

This study shows the importance of considering both the type of simulation model used and the proper inclusion of relevant physical phenomena and boundary conditions, when modelling the interaction between planets and the solar wind. Although the different models agree fairly well in terms of macroscopic plasma parameters they produce ENA images that differ substantially.

Key words: solar wind-Mars interaction, energetic neutral atoms (ENA), charge exchange, ENA imaging, MHD, hybrid simulation
PACS: 52.65.Kj, 52.65.Ww, 96.30.Gc, 96.35.Hv

1 Introduction

Energetic neutral atoms (ENAs) are produced by solar wind protons and newly created planetary ions that undergo charge exchange collisions with neutral atoms in the exospheres of the non-magnetised planets. In the past no ENA imaging of Mars have been done in the solar wind energy range (below 10 keV for hydrogen). The first ENA images of the Mars-solar wind interaction region will be collected by the ASPERA-3 (Analyzer of Space Plasmas and Energetic Atoms) instrument on board ESA's Mars Express mission that will begin to return data from an orbit around Mars in early 2004 (Barabash et al., 2004b). ASPERA-3 has two ENA imagers, the neutral particle imager (NPI) with higher angular resolution, but no energy resolution, and the neutral particle detector (NPD) with energy and mass resolution, but crude angular resolution.

In this work three different models of the interaction between the solar wind and Mars are examined, with emphasis on the generation of ENA images. A comparison between ENA images of Mars and Venus is made in a companion paper (Gunell et al., 2004). The purpose of comparing different simulation models is twofold. Firstly, we wish to find out how the choice of plasma model influences the simulated ENA images. This will aid in choosing the right model for ones simulation needs. Secondly, comparing the models sheds light on which, and how, underlying physical principles and assumptions influence the images. This knowledge will be important when measured images from spacecraft-based instruments are to be interpreted.

The three models examined here are:

(1) an empirical model that is based on Phobos 2 measurements (Kallio et al., 1997),
(2) a three dimensional hybrid simulation (Kallio and Janhunen, 2001, 2002), and
(3) a three-dimensional MHD simulation (Ma et al., 2002).

For the ENA calculation we use a Chamberlain exosphere to model the neutral gas density. The same exosphere model is used for all the three plasma models. Fig. 1 shows the neutral gas density as a function of altitude. The number

* Corresponding author
Email address: herbert.gunell@physics.org (H. Gunell).

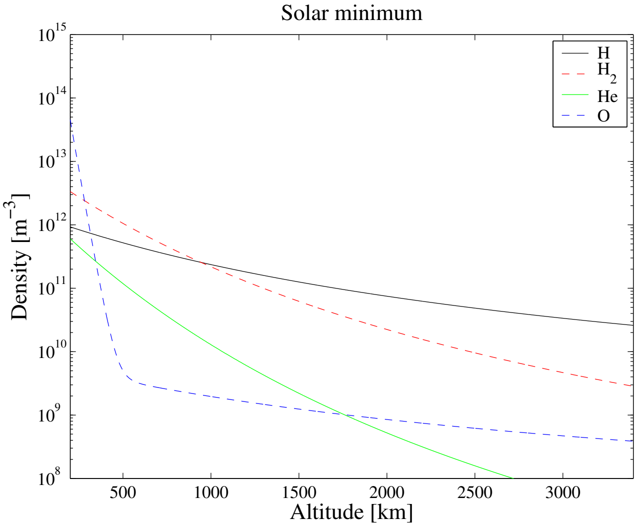

Fig. 1. Neutral gas densities as a function of altitude for the dominant neutral species in the upper atmosphere of Mars. Of these H, H_2, and O are important for the generation of energetic neutral atoms. The contribution from helium is negligible because of its very small cross section for charge exchange collisions.

density n_i of neutral species i is modelled as

$$n_i = N_i e^{-\beta_i \left(\frac{1}{r_0} - \frac{1}{r}\right)} \zeta(\beta_i / r) \tag{1}$$

where r is the distance to the centre of Mars, r_0 is the radius of the exobase, ζ is Chamberlain's partition function (Chamberlain and Hunten, 1987), and β_i is a constant that is determined by the mass and temperature of each species

$$\beta_i = \frac{GMm_i}{k_B T_i} \tag{2}$$

where G is the gravitational constant, $M = 6.46 \cdot 10^{23}$ kg is the mass of Mars, m_i is the atomic mass of neutral species i, and T_i is the temperature of species i at the exobase. The parameters have been adopted from Kallio et al. (1997); Holmström et al. (2002); Krasnopolsky and Gladstone (1996). An exobase altitude of 170 km is used throughout this report. The other parameters are shown in Table 1.

For hydrogen, only ENAs with energies above 50 eV are considered here, since the contribution from lower energies is small (Holmström et al., 2002) and because the assumption that a newly produced ENA has the same momentum as the incident proton is not valid for low energies (Hodges and Breig, 1991). For oxygen the lower energy limit is set to 100 eV in accordance with Barabash et al. (2002a).

The solar wind parameters that are used throughout this report follow those used by Ma et al. (2002) as closely as possible, and are shown in Table 2. The

Table 1
Parameters of the neutral gas density model (Kallio et al., 1997; Holmström et al., 2002; Krasnopolsky and Gladstone, 1996). The exobase is located at 170 km altitude.

Species	N_i	T_i
H	$9.9 \cdot 10^{11}$ m^{-3}	192 K
H_2	$3.8 \cdot 10^{12}$ m^{-3}	192 K
He	$7.2 \cdot 10^{11}$ m^{-3}	275 K
O_{hot}	$5.5 \cdot 10^{9}$ m^{-3}	$4.4 \cdot 10^{3}$ K
$O_{thermal}$	$1.4 \cdot 10^{14}$ m^{-3}	173 K

neutral gas densities used when computing the ENA images are shown in Fig. 1. The coordinate system that is used in this report has its origin in the centre of Mars, the Sun in the positive x-direction, the z-axis is northernly directed and perpendicular to the ecliptic. The y-direction closes the right-handed system. A schematic explaining the coordinate system and the directions of the solar wind velocity, electric and magnetic fields is shown in Fig. 2.

2 Description of the models

2.1 The empirical model

An empirical model for the plasma flow around Mars based on measurements made with the ASPERA (Automatic Space Plasma Experiment with a Rotating Analyzer) instrument on board the Phobos 2 spacecraft was developed by Kallio (1996). This model was used to study the production of energetic neutral atoms through charge exchange collisions between the solar wind protons and atoms and molecules in the Martian neutral atmosphere (Kallio et al., 1997). It has also been used to study the motion of protons and oxygen ions near Mars (Kallio and Koskinen, 1999). The model is cylindrically symmetric with respect to the Mars-Sun axis, and includes a bow shock and a magnetic

Table 2
Solar wind parameters

Plasma density	$4 \cdot 10^{6}$m^{-3}	
Temperature	$1.75 \cdot 10^{5}$K	(mean of $5 \cdot 10^{4}$ K protons and $3 \cdot 10^{5}$ K electrons)
Solar wind speed	500 km/s	
Magnetic flux density	3 nT	direction: $(x, y, z) = (cos(56°), sin(56°), 0)$

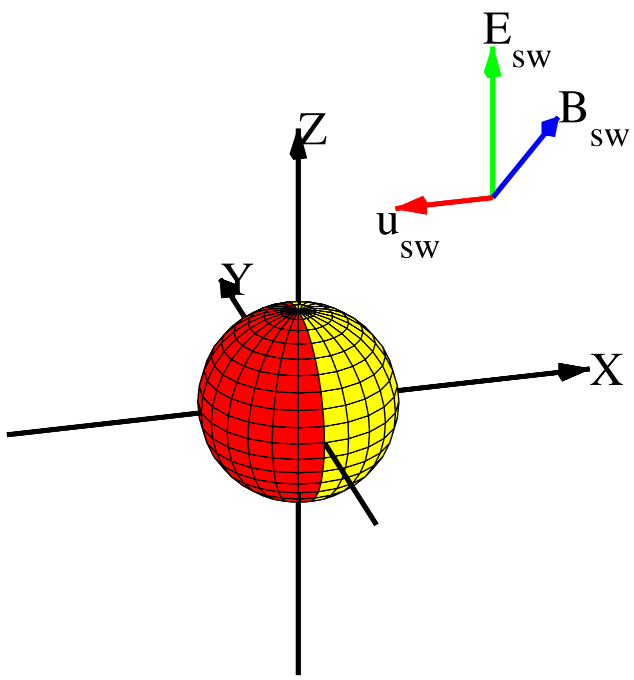

Fig. 2. Schematic of the simulated system, with the coordinate axes and the directions of the solar wind velocity, electric and magnetic fields shown. The sun is in the positive x-direction, the z-axis is northernly directed and perpendicular to the ecliptic. The y-direction closes the right-handed system.

pileup boundary. The magnetic field is frozen into the modelled flow. A spherical obstacle, that is impenetrable to the flow, is assumed at 170 km altitude. The model is parameterised, and the parameter values used here are the same as those used by Holmström et al. (2002). The bow shock shape is given by a conical function that is based on Mariner 4, Mars 2, 3, 5, and Phobos 2 bow shock crossings. The planetocentric distance of the nose of the bow shock is $1.55R_m$. The shape of the magnetic pileup boundary is given by an even fourth order polynomial based on Phobos 2 data, and the nose of the magnetic pileup boundary is at $1.2R_m$ planetocentric distance.

Hydrogen ENA images from the empirical model were computed and published by Holmström et al. (2002). They calculated the ENA emission by combining the empirical model of the plasma flow with a model for the neutral gas density of the Martian atmosphere, using cross sections for the relevant charge exchange reactions. The ENA images are then generated by integrating the ENA emission along lines of sight to a virtual ENA instrument. This approach does not self-consistently account for the loss of ions when ENAs are produced. The integration path is limited by a sphere of radius $20R_m$ centred at Mars. The proton temperature is given by an analytical approximation from gas dynamics (Kallio et al., 1997). The hydrogen ENA images from the empirical model are discussed further in section 3.1.

A similar approach was used by Barabash et al. (2002a) to generate oxygen ENA images; the difference being that the distribution of oxygen ions was given by a test particle simulation, where trajectories of oxygen ion test particles moving in the electric and magnetic fields of the empirical model were calculated. With knowledge of the O^+ distribution function, the neutral gas density profiles in the vicinity of Mars and the cross sections for charge exchange the ENA emission can now be calculated. The ENA images are then obtained by integration of the ENA emission along lines of sight. Oxygen ENA images from the empirical model are discussed further in section 3.2.

2.2 The hybrid model

A three-dimensional hybrid simulation code was developed by Kallio and Janhunen (2001, 2002). In the hybrid model the ions are treated as particles, the motion of which are governed by the Lorentz force. The electrons are treated as a massless neutralising fluid. In this paper an ion in the hybrid model is called as a "super-ion" because an ion in the simulation corresponds to a large number of real ions. The resulted ENA is therefore also a "super-ENA" because it represents many real ENAs. The super-ions have the same mass to charge ratio as the ion species they represent. The magnetic field is assumed to be frozen into the electron fluid. No assumptions are made about the temperature, bulk velocity, or the shape of the distribution function. Finite gyro radius effects and Hall effects are included in the model.

The simulation is performed on a non-uniform grid, that has a grid spacing of 720 km $\approx 0.2R_m$ in most of the simulated region. Closer to Mars, on its dayside, a finer grid, with spacing 360 km $\approx 0.1R_m$ and 180 km $\approx 0.05R_m$ is used. The simulation box is a Mars-centred cube: $-3R_m < x, y, z < 3R_m$, and an obstacle boundary is assumed at $r = R_{obst} = 3600$ km. Fully absorbing boundary conditions are imposed at the obstacle boundary and at the boundary of the simulation box, i.e., ions that hit the obstacle or the edge of the simulation box are removed from the simulation. There are three different ion species included in the simulation; H^+, O^+, and O_2^+. There are two sources of planetary ions: photo-ionisation of the neutral corona and emissions of ionospheric ions from the obstacle boundary. The Martian crustal magnetic fields are not included in the version of the model that is under consideration here. The number of super-particles per grid cell is about 20, but it can vary for the different ion species. This means that it is possible that some species may be represented by an insufficient number of super-particles, particularly near the ionosphere. The work on refining the ionosphere model is ongoing.

The hybrid code self-consistently includes four charge exchange reactions, namely

(1) $H^+ + O \rightarrow H + O^+$,
(2) $O^+ + O \rightarrow O + O^+$,
(3) $H^+ + H \rightarrow H + H^+$, and
(4) $O^+ + H \rightarrow O + H^+$.

The hybrid model produces a bow shock and piling up of the magnetic field against the planet on its dayside. This is typically referred to as a magnetic barrier or as a magnetic pile up boundary, MPB, in the Mars and Venus literature. A magnetotail is formed downstream of the planet, much as in the empirical model. See Kallio and Janhunen (2001) and (Kallio and Janhunen, 2002), for a comparison between the hybrid model and the empirical model.

The hybrid code is able to generate its own discrete ENAs since the position and velocity of all super-ions are known at each time step. The probability for an ion to have a charge exchange collision is then found from the neutral density and the energy dependent cross section. An energetic super-ion is taken away from the simulation in proportion to the probability of a charge exchange collision, and it is then replaced by a newly born super-ion which has the same weight as the original energetic super-ion. Charge exchange collisions are thus accounted for self-consistently. The super-ion velocities, positions, and weights are saved periodically. The images are generated after the completion of the simulation from the information in those files. Using the neutral model described above and the charge exchange cross sections the ENA flux caused by each super-ion in the files is computed, and the contributions of the thus formed super-ENAs to the ENA flux into a virtual ENA instrument are calculated.

2.3 The MHD model

The ENA images presented in section 5 are based on the ion flow results obtained from an MHD simulation by Ma et al. (2002). In MHD the plasma is treated like a fluid, and the magnetic field is frozen into that fluid. The present MHD model uses three separate continuity equations for H^+, O_2^+, and O^+, but only one momentum equation and thus assumes that all ions have the same velocity. A Maxwellian velocity distribution is assumed implicitly, by the use of the moment equations. The interaction with the neutral exosphere, and the production of an ionosphere through ionisation is modeled by including source and loss terms for O_2^+ and O^+, but not for H^+. The simulation box is defined by $-24R_m \leq x \leq 8R_m$, $|y| \leq 16R_m$, $|z| \leq 16R_m$. The grid is nonuniform with a grid size of $2R_m$ far from the planet on the nightside, and as small as $R_m/64$ close to the planet.

The crustal magnetic fields of Mars were included in the simulations by the

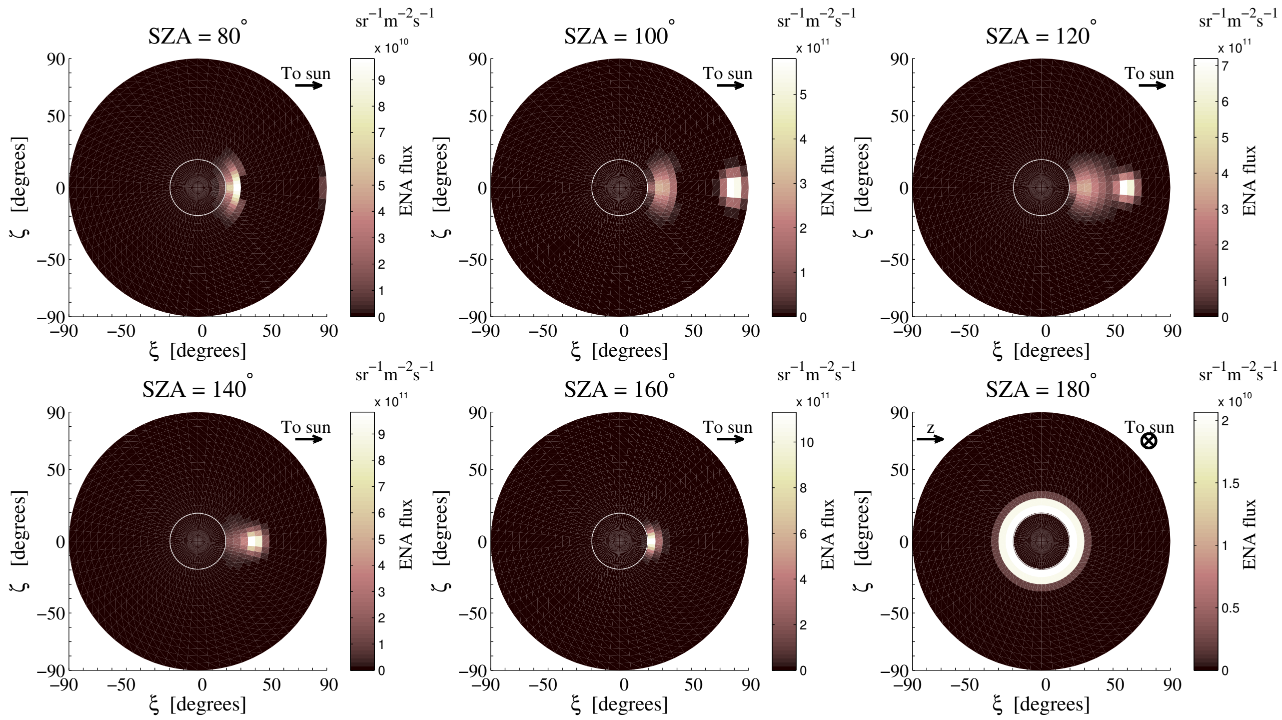

Fig. 3. Hydrogen ENA-images from the empirical model. The ENA images shown are from vantage points $3R_m$ from the centre of Mars, looking down at the planet. The solar zenith angles are, from left to right starting in the upper row; 80°, 100°, 120°, 140°, 160°, and 180°. The colour scale shows the ENA flux in units of $\mathrm{sr}^{-1}\mathrm{m}^{-2}\mathrm{s}^{-1}$. The horizontal axis ξ and the vertical axis ζ show the angular offset in degrees, from the centre of the image.

use of a 60-degree expansion based on Mars Global Surveyor data (Arkani-Hamed, 2001). The inclusion of the crustal magnetic fields is seen to affect the location of the ionopause (Ma et al., 2002).

ENA images from the MHD model are generated in the same way as with the empirical model. The flows of hydrogen and oxygen ions are given by the output of the MHD code and these are combined with the models of the neutral gas densities and cross sections.

3 Results from the empirical model

3.1 Hydrogen ENA images (empirical model)

The ENA images were calculated by integrating the ENA production along lines of sight as described by Holmström et al. (2002). Fig. 3 shows hydrogen ENA images from vantage points in the xz-plane, three Mars radii (R_m) away

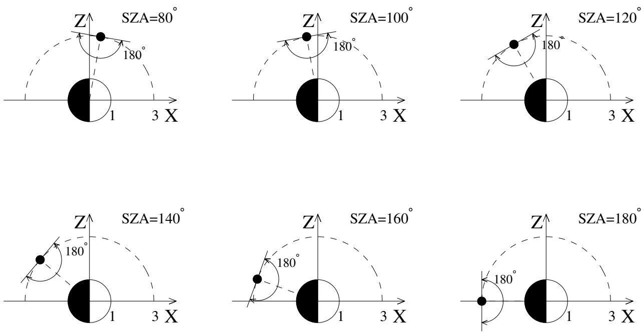

Fig. 4. Illustration of the vantage points and fields of view in the hydrogen ENA images (figures 3, 9, and 12).

from the centre of Mars. The vantage points and their fields of view are illustrated in Fig. 4. Due to the cylindrical symmetry of the model the images from all vantage points with the same solar zenith angle and planetocentric distance are identical. The structure and shape of the images are in reasonable agreement with the images from the MHD model, although the absolute values of the ENA flux are slightly lower in the images produced by the empirical model. There are two maxima in the ENA flux; one produced upstream in the solar wind and another closer to, but separated from, the planet. The ENAs that are produced in the solar wind, via charge exchange of solar wind protons and planetary exospheric hydrogen, are dominating in those of the images where the direction toward the Sun is within the field of view. This is because we are then looking directly into the solar wind flow. When the plasma flow is not directed straight at our virtual instrument we only collect ions moving at an angle to the flow velocity due to the plasma temperature. The length of the integration path is also an issue related to the magnitude of the computed ENA flux. For the empirical model the ENA production is integrated inside a sphere of radius $20R_m$ centred at Mars. The proton temperature is given by an analytical approximation from gas dynamics (Kallio et al., 1997).

The images were obtained by integrating along lines of sight from a virtual ENA instrument. A Maxwellian velocity distribution of the solar wind protons was assumed.

3.2 Oxygen ENA images (empirical model)

The oxygen ion distribution function has been estimated by a test particle simulation (Barabash et al., 2002a). The source, giving the initial distribution, of O^+ test particles was photo-ionised oxygen from the exosphere. The test particles move under the influence of the solar wind magnetic field and the induced electric field $\vec{E} = -\vec{v} \times \vec{B}$, assuming frozen-in field lines, and the flow velocity being given by the empirical flow model (Kallio, 1996). The

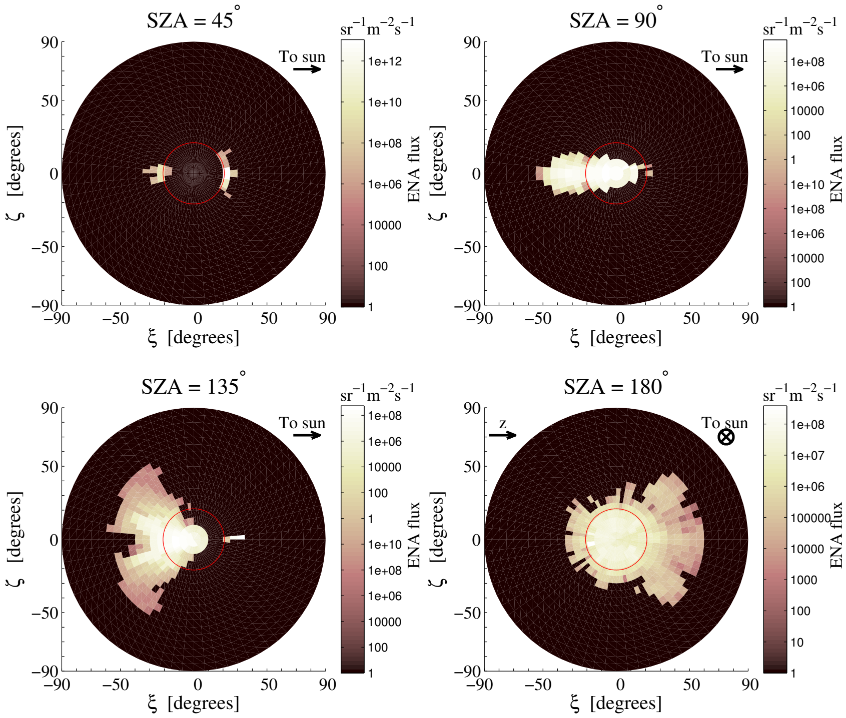

Fig. 5. Oxygen ENA-images from the empirical model. The images shown are from vantage points in the xz-plane ($z \geq 0$), $3R_m$ from the centre of Mars, looking down at the planet. The solar zenith angles are 45°, 90°, 135°, and 180°. The colour scale shows the ENA flux in units of $\mathrm{sr}^{-1}\mathrm{m}^{-2}\mathrm{s}^{-1}$, on a logarithmic scale. The horizontal axis ξ and the vertical axis ζ show the angular offset in degrees, from the centre of the image.

trajectories of the ions are calculated first, and from those trajectories the six-dimensional distribution function is calculated in a simulation box that in physical space is $4R_m \times 4R_m \times 4R_m$ and centred on Mars.

With knowledge of the O^+ distribution function, the neutral gas density profiles in the vicinity of Mars and the cross sections for charge exchange the ENA emission can now be calculated. The ENA images are then obtained by integration of the ENA emission along lines of sight. Because of the limited number of O^+ ions in the test particle simulation, the number of points in velocity space where the distribution function is known is relatively small. This makes it difficult to accurately integrate over energy. An estimate can be made, however, and it is shown in Fig. 5, which includes the contribution from oxygen ENAs with energies over 100 eV. The figure shows oxygen ENA images from vantage points in the xz-plane, three Mars radii away from the centre of Mars. The vantage points and their fields of view are illustrated in Fig. 6. The colour scale is logarithmic since the images otherwise would be dominated by a few bright spots, due to the small number of test particles.

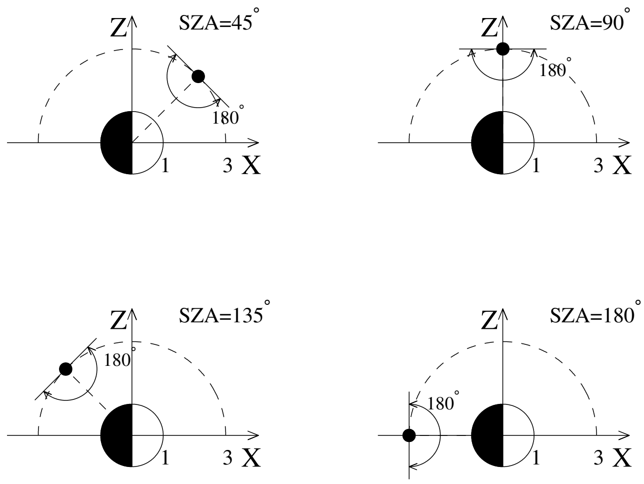

Fig. 6. Illustration of the vantage points and fields of view in the oxygen ENA images (figures 5, 10, and 13).

3.3 ENA production (empirical model)

The production rate for hydrogen ENAs is shown in the upper panel of Fig. 7. The production rate has been integrated over the azimuthal coordinate. In the empirical model the maximum is located about one Mars radius off the x-axis, and the ENA production on the x-axis above the sub-solar point is small. The maximum in the ENA production is clearly separated from the planet, a fact that also can be seen in the ENA images (Fig. 3).

4 Results from the hybrid simulation

4.1 Density distribution (hybrid model)

Barabash et al. (2002a) used a test particle simulation with $\vec{E}$- and $\vec{B}$-fields from the empirical model to calculate column densities, i.e., densities integrated across the simulation box along one of the coordinates, and found a maximum of the oxygen ion density above the northern hemisphere (or the $+\vec{E}_{sw}$ hemisphere, since the solar wind electric field is northernly directed). In the previously published run of this hybrid simulation code (Kallio and Janhunen, 2002), as well as in the run presented here, the maximum O^+ density is on the southern side of Mars, i.e. on the $-\vec{E}_{sw}$ side. Fig. 8 shows the O^+ density in the xz-plane of the hybrid simulation. There is an O^+ density minimum at the sub-solar point due to a northward acceleration of oxygen ions. The density has its maximum on the southern side of the planet. This is most evident on the nightside, where a large southernly region of high O^+

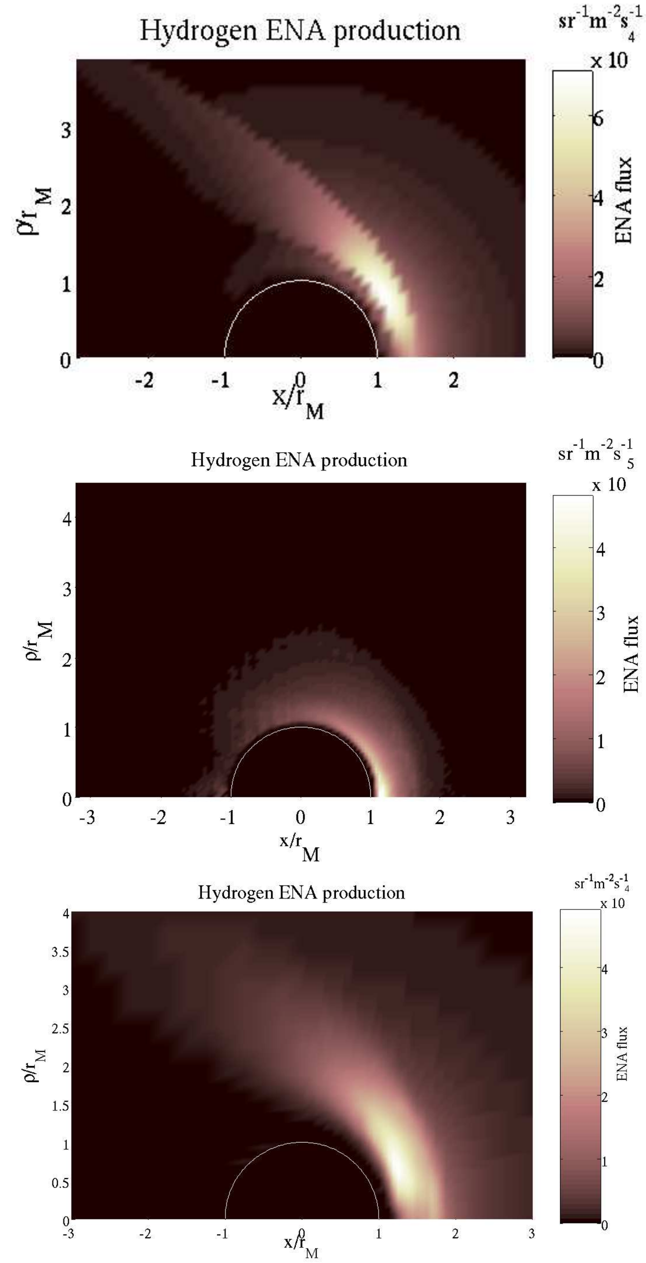

Fig. 7. Production of hydrogen ENAs in the empirical (top panel), hybrid (middle panel), and MHD models (bottom panel). The colour-coded production rate has been integrated over the azimuthal angle, and is given in units of $m^{-3}s^{-1}$. The cylindrical coordinate $\rho = \sqrt{y^2 + z^2}$ is the distance from the Mars-Sun line.

density can be seen. The distribution of ions is influenced by the ion sources. In the hybrid simulation there is an assumed emission of O^+ ions from the ionosphere of $1.4 \cdot 10^{25}$ oxygen ions per second, and a $2 \cdot 10^{25} s^{-1}$ emission of O_2^+. There is no such ionospheric plasma source in the test particle simulation of oxygen ions in the fields produced by the empirical model (Barabash et al., 2002a).

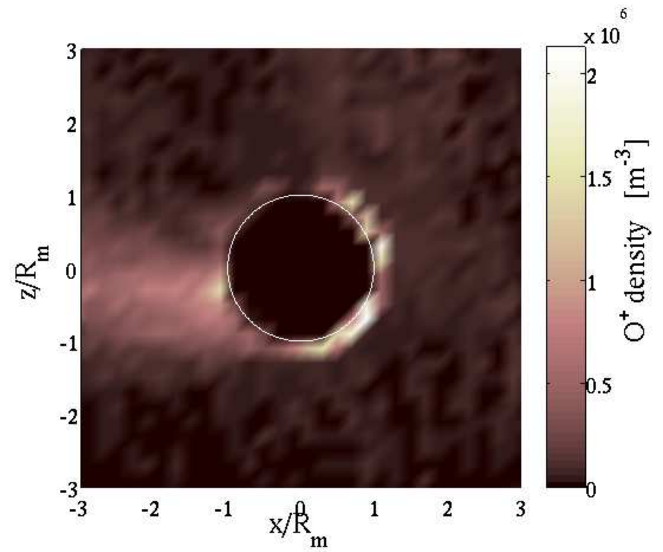

Fig. 8. O^+ density in the xz-plane for the the hybrid code. Oxygen ions that are emitted from the ionosphere, are the likely cause for the position of the O^+ density maximum. The density is shown in units of m^{-3}.

4.2 ENA images (hybrid model)

The positions, velocities and weights of all super-particles in the simulation are periodically saved in dump files every five seconds starting at time $t = 200$ s and ending at $t = 245$ s, when ten files have been saved. Knowing the neutral exospheric densities and the energy dependent charge exchange cross sections the ENA production rate for each super ion can easily be calculated. The number of ENAs per second generated by the ith proton is

$$q_i = w_i v_i \sum_{\alpha} N_\alpha(\vec{r}_i)\sigma_\alpha(v_i) \tag{3}$$

where w_i is the number of real protons that are represented by super-proton i, $N_\alpha(\vec{r}_i)$ is the density of neutral gas species α at the position $\vec{r}_i$ of proton i, and $\sigma_\alpha(v_i)$ is the cross section for charge exchange collisions between a proton with speed v_i and a neutral particle of species α (Kallio et al., 1997; Barabash et al., 2002a).

The newly produced ENAs are assumed to travel with the same velocity as the incident ion, and those that hit a virtual ENA detector are collected in bins depending on their respective incident angles. For the pictures presented here the radius of the "ENA camera" is $0.2R_m$ for the hydrogen images and $0.5R_m$ for the oxygen images. The non-zero radius of the virtual instrument introduces an error since particles on parallel trajectories arriving to different parts of the virtual instrument with the same incident angle will be counted in the same pixel, even though the locations of their respective sources are

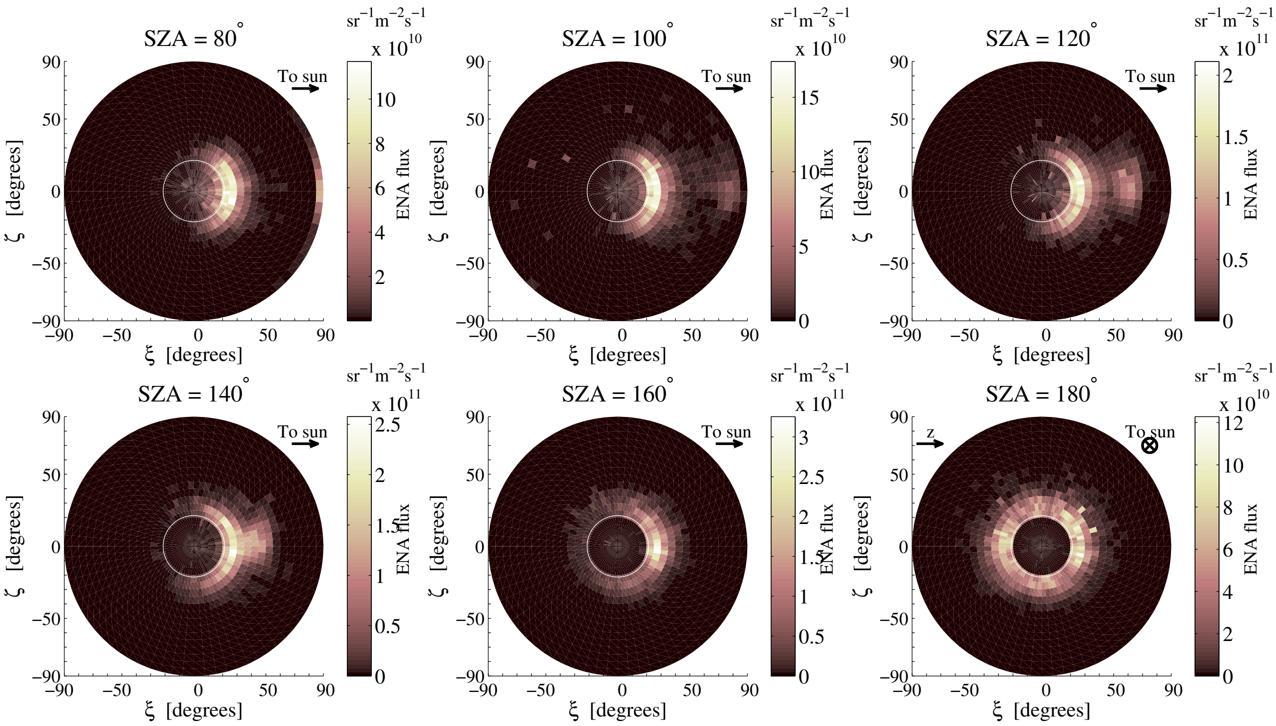

Fig. 9. Hydrogen ENA-images produced by the hybrid model. Mars is viewed from vantage points in the xz-plane ($z \geq 0$), three Martian radii from the centre of Mars. From left to right, starting at the upper left panel, the solar zenith angles of the vantage points are $80°, 100°, 120°, 140°, 160°$, and $180°$. The colour scale shows the ENA flux in units of $\mathrm{sr}^{-1}\mathrm{m}^{-2}\mathrm{s}^{-1}$. The horizontal axis ξ and the vertical axis ζ show the angular offset in degrees, from the centre of the image.

different. A virtual instrument radius of $0.2R_m$ is consistent with the $5° \times 5°$ pixel size used in the ENA images. The larger radius in the oxygen case is necessary due to the smaller number of oxygen super-particles. Finally the images from the ten dump files are averaged.

An ENA production boundary at 3700 km planetocentric distance, below which no ENAs are produced, ($\approx$ 300 km height) has been assumed when calculating the ENA images. This is because the number of super-particles inside that boundary is so small in the simulation that including those would produce unrealistic results. The number density of super-particles must not be too small or else the particle discreteness will produce a spotty picture. If this happens in a region with low neutral density the error is not significant, since then the produced ENA flux is small anyway, but inside 3700 km the neutral density is high and there is a significant ENA production.

Hydrogen ENA images generated from the same vantage points as the images published by Holmström et al. (2002) are shown in Fig. 9. A local maximum on the right hand side of the pictures representing ENAs produced upstream in the solar wind can be seen. The contribution from the solar wind upstream

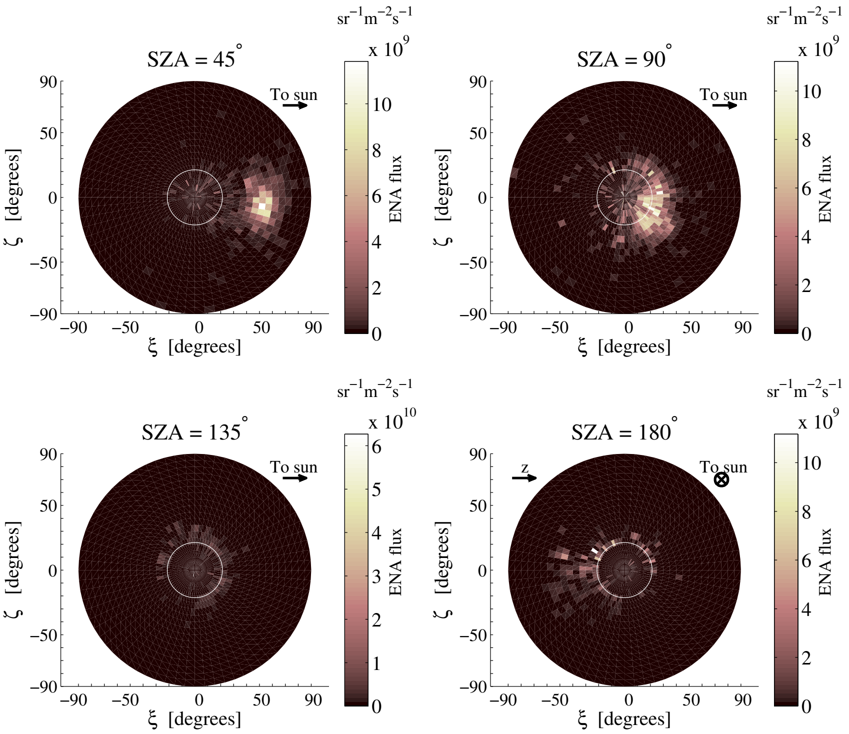

Fig. 10. Oxygen ENA-images from the hybrid model. Mars is viewed from a vantage point in the xz-plane ($z \geq 0$), three Martian radii from the centre of Mars. From left to right, starting at the upper left panel, the solar zenith angles of the vantage points are 45°, 90°, 135°, and 180°. The colour scale shows the ENA flux in units of sr^{-1}m^{-2}s^{-1}. The horizontal axis ξ and the vertical axis ζ show the angular offset in degrees, from the centre of the image.

of the bow shock is smaller in the hybrid model than in the other two models because of the size of the simulation box. It only reaches three Mars radii from the centre of Mars in the x-direction, and thus the contributions from charge exchange reactions taking place further away are not included. In the MHD simulation the simulation box goes out to $x = 8R_m$, and in the empirical model the integration is performed out to twenty Mars radii.

Fig. 10 shows oxygen ENA images, including oxygen ENAs with energies exceeding 100 eV. The asymmetry in the oxygen images is a result of the asymmetry in the O^+ density. This is most easily seen from the lower right panel of Fig. 10, where the vantage point is above the anti-solar point. Since the asymmetry in the ion density can be seen in the oxygen ENA image, such images can be used to remotely measure asymmetries in the global distribution of oxygen ions. In the two upper panels of Fig. 10 there is another asymmetry. The maximum ENA flux is located in the lower half of the images. This means that the maximum emission comes from a volume that is not centred on $y = 0$, but displaced toward negative values of y. Such asymmetries are introduced by the solar wind magnetic field, which is tilted 34° with respect to the y-axis.

4.3 ENA production (hybrid model)

The production rate for hydrogen ENAs is shown in the middle panel of Fig. 7. The production rate has been integrated over the azimuthal coordinate. In the hybrid simulation considered here the maximal production rate appears on the x-axis on the dayside of Mars, whereas in the empirical and MHD models the maxima are located about one Mars radius off axis, c. f., sections 3.3 and 5.3.

Apart from reaching the axis rather than being annular the production region in the hybrid simulation also shows a production rate several times higher than the production rate in the empirical model. Compared with the empirical model the ENA production maximum is much closer to the planet in the hybrid model. This is a result of the coarse grid used in the hybrid simulation.

5 Results from the MHD simulation

5.1 Density distribution (MHD model)

Fig. 11 shows the densities in the xz-plane for the protons (left panel), O^+ ions (middle panel). The MHD simulation resolves much higher O^+ densities close to the Martian surface than the hybrid code does, and hence the right panel of Fig. 11 is dominated by the region closest to the planet. This is also true for the O_2^+ ion density (not shown). The rightmost panel of Fig. 11 shows the O^+ ion density in the xz-plane on the nightside of Mars. A slightly higher density can be seen on the northern $(+\vec{E}_{sw})$ side, that is opposite to the hybrid simulation that has its maximum on the $-\vec{E}_{sw}$ side. The difference between the models in this respect is probably due to the inclusion of the crustal magnetic fields effects in the MHD model. In the hybrid model the crustal magnetic fields are absent. Also, the Hall term and finite gyro-radius effects are treated self-consistently in the hybrid but not in the MHD model. The differences in the ion density distributions are also influenced by how the ions are created in the different models.

5.2 ENA images (MHD model)

The ENA images from the MHD model were calculated in the same way as those of the empirical model described in section 3.1 and in detail by Holmström et al. (2002). The plasma flow and temperature values are obtained from

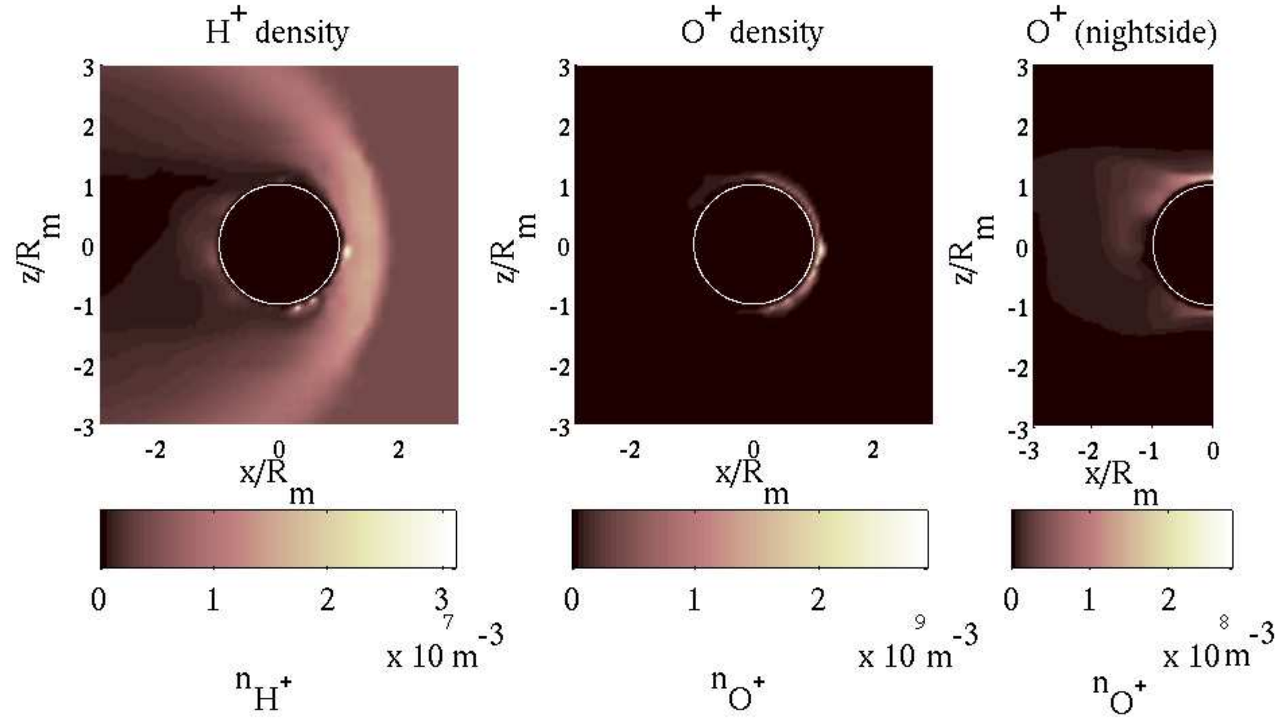

Fig. 11. Densities in the xz-plane of the MHD model for the protons (left panel) and O^+ ions (middle panel). The right panel shows the O^+ ion density in the xz-plane on the nightside of Mars. The number density is shown in units of m^{-3}.

the output files from the run of the MHD code. When evaluating the line of sight integrals linear interpolation of the values known at the grid points is performed. Fig. 12 shows hydrogen ENA images from vantage points in the xz-plane ($z \geq 0$), three Mars radii away from the centre of Mars, and with solar zenith angles 80°, 100°, 120°, 140°, 160°, and 180°. In the first panel the solar zenith angle is 80° and two local maxima in the ENA flux can be seen. The maximum at the right hand side of the figure represents ENAs produced in the solar wind. There is also a local maximum close to, but separated from, the planet. As the vantage point is moved toward the nightside of Mars in the subsequent panels the maximum associated with ENAs produced upstream in the solar wind moves toward the centre of the image and is dominating over the other maximum. That the maximum ENA flux is separated from the planet shows that the magnetic pileup boundary that appears in the MHD simulation also can be detected in ENA images. The emissions from the MHD model are more concentrated than those from the hybrid model (Fig. 9), that are spread out over a larger region. There are thus differences between the models that spacecraft-based ENA instruments should be able to detect.

Fig. 13 shows oxygen ENA images from vantage points in the xz-plane ($z \geq 0$), three Mars radii away from the centre of Mars, and solar zenith angles 45°, 90°, 135°, and 180°. As with the hydrogen ENAs the oxygen ENA emissions

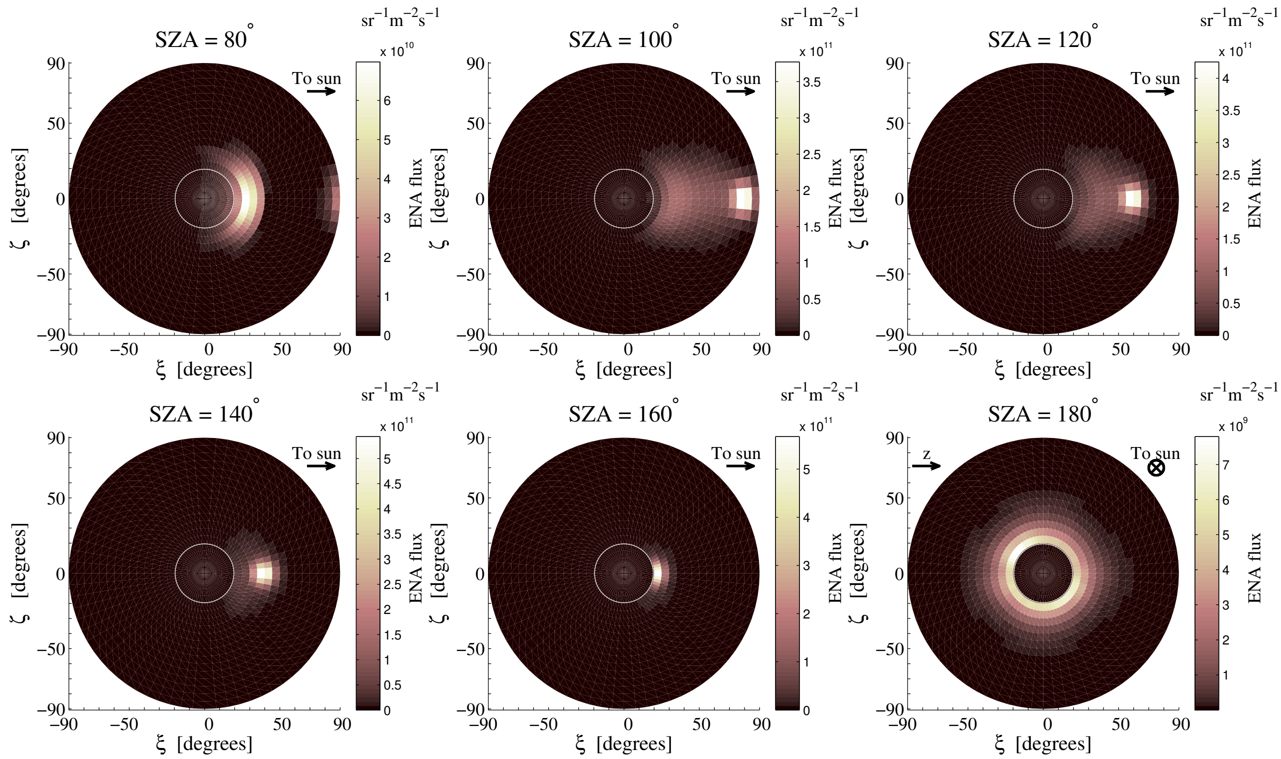

Fig. 12. Hydrogen ENA-images produced by the MHD model. Mars is viewed from a vantage point in the xz-plane ($z \geq 0$), three Martian radii from the centre of Mars. From left to right, starting at the upper left panel, the solar zenith angles of the vantage points are 80°, 100°, 120°, 140°, 160°, and 180°. The colour scale shows the ENA flux in units of sr^{-1}m^{-2}s^{-1}. The horizontal axis ξ and the vertical axis ζ show the angular offset in degrees, from the centre of the image.

in the MHD model are more concentrated to the interaction region close to the dayside of the planet, whereas the hybrid model produces more emissions that are spread out over a larger area. This is a finite gyro-radius effect, the oxygen gyro-radius being of the same order of magnitude as the radius of the planet.

The image from SZA=180° shows maxima both north and south of the planet of approximately the same intensity, which is consistent with the MHD model having only a small north-south asymmetry in the oxygen ion density. The corresponding image from the hybrid model shows an asymmetry that is consistent with the asymmetrical oxygen ion density distribution of that model.

5.3 ENA production (MHD model)

The production rate for hydrogen ENAs is shown in bottom panel of Fig. 7. It has been integrated over the azimuthal coordinate for comparison with the

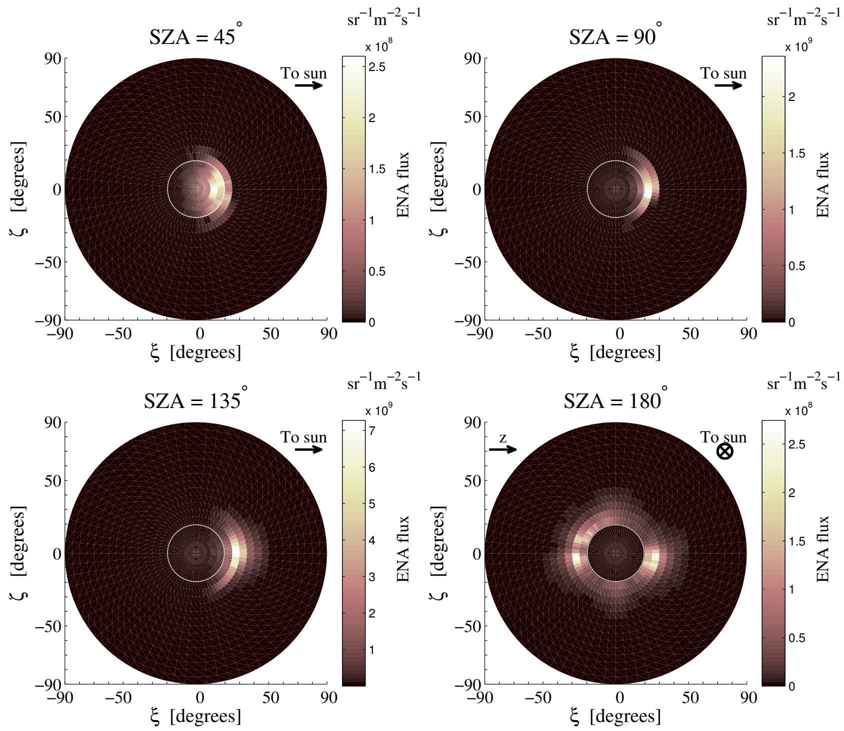

Fig. 13. Oxygen ENA-images from the MHD model. Mars is viewed from a vantage point in the xz-plane ($z \geq 0$), three Martian radii from the centre of Mars. From left to right, starting at the upper left panel, the solar zenith angles of the vantage points are 45°, 90°, 135°, and 180°. The colour scale shows the ENA flux in units of sr^{-1}m^{-2}s^{-1}. The horizontal axis ξ and the vertical axis ζ show the angular offset in degrees, from the centre of the image.

results of the other models. The global maximum is located off the Mars-Sun line like it is in the empirical model, however a significant production rate is found on the Mars-Sun line like it is in the hybrid model. The region with a high ENA production rate is located further away from the planet in the MHD and empirical models than in the hybrid model, due to the presence of a well resolved magnetic pileup boundary in the empirical model and in the MHD results.

6 Summary and conclusions

We have simulated ENA images based on three different models of the plasma flow around Mars. Fig. 14 shows three ENA images from each model. These images are the images from solar zenith angles 100°, 140°, and 180° that are also shown in figures 3, 9, and 12. In Fig. 14 the left column shows ENA images from the empirical model, the middle column the hybrid model, and the right column shows ENA images from the MHD model. The colour scales are the same for panels on the same row to enable a quantitative comparison

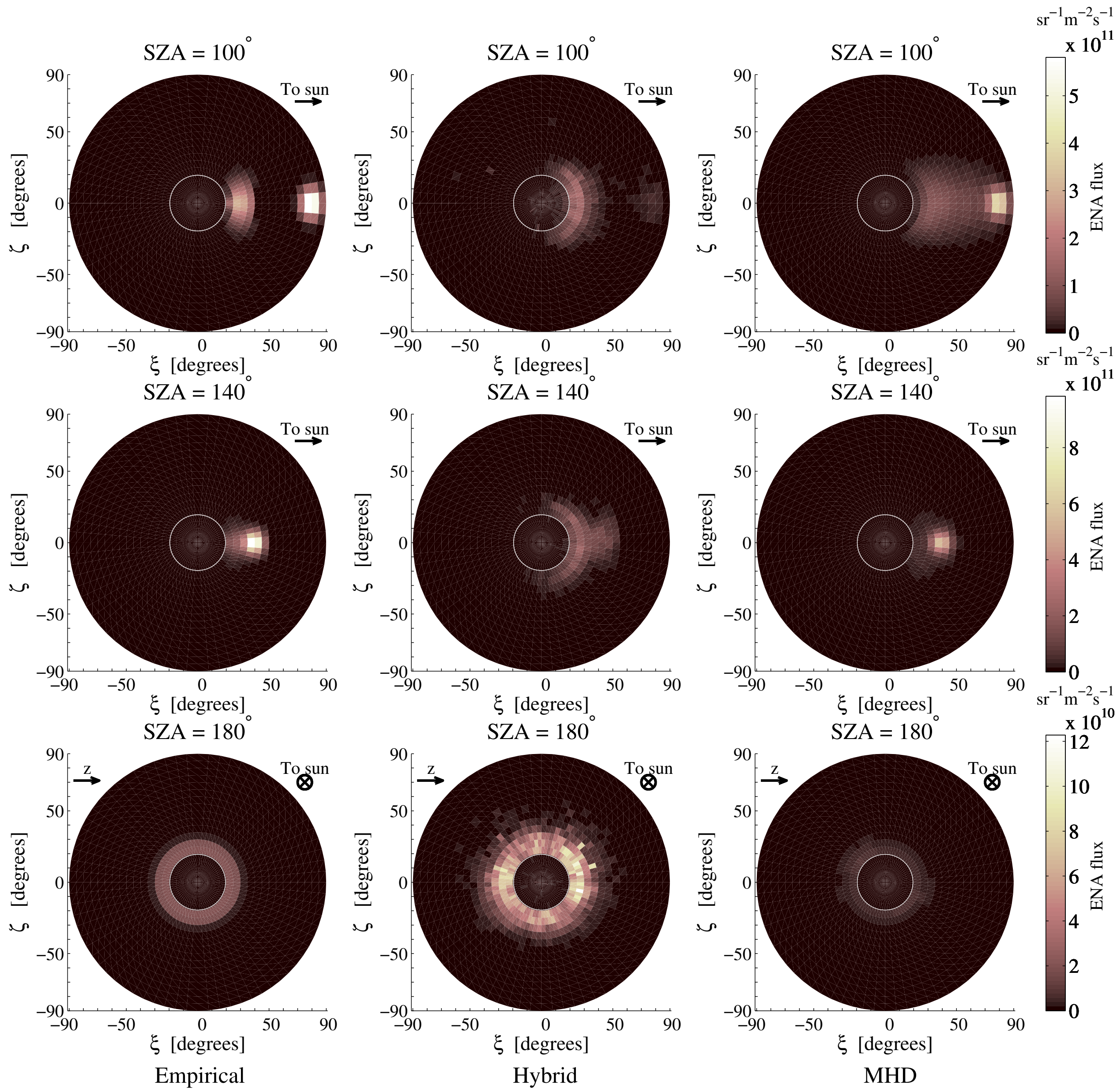

Fig. 14. Hydrogen ENA images from the three models. The left column shows ENA images from the empirical model, the middle column the hybrid model, and the right column shows ENA images from the MHD model. Panels that are on the same row show images from the same vantage point, i.e. a vantage point in the xz-plane ($z \geq 0$), $3R_m$ from the centre of Mars, and a solar zenith angle of 100° (upper row), 140° (middle row), and 180° (bottom row). The colour scales are the same for panels on the same row.

between the models.

It can be seen in the top row, where the solar zenith angle is 100°, that the observed flux of ENAs produced in the solar wind is lowest in the hybrid model. This, as has been pointed out in previous sections, is a result of the smaller

Table 3
A comparison of some aspects of the results of the different models. The solar wind hydrogen ENA flux are taken from the images with a solar zenith angle of 100°. The total hydrogen ENA production was calculated by integrating the ENA production within a cylinder oriented along the x-axis from $x = -3R_m$ to $x = 3R_m$, and with a radius $\rho = 3R_m$.

	Empirical	Hybrid	MHD	unit
Solar wind H-ENA flux	$5.8 \cdot 10^{11}$	$3.3 \cdot 10^{10}$	$3.8 \cdot 10^{11}$	$\mathrm{sr}^{-1}\mathrm{m}^{-2}\mathrm{s}^{-1}$
Total H-ENA production	$2.7 \cdot 10^{25}$	$5.8 \cdot 10^{25}$	$2.4 \cdot 10^{25}$	s^{-1}

simulation box used in that model. It can also be seen that the upstream maximum is about 50 % stronger in the empirical (top left panel) than in the MHD model (top right panel). The reason for this is that the integration is carried out all the way to $20R_m$ planetocentric distance in the empirical model, and only to the end of the simulation box at $x = 8R_m$ in the MHD model. The bow shock position and the discretisation of the images also influence the exact value.

From the bottom row in Fig. 14 it is seen that the hybrid model produce a much larger ENA flux than the other models when Mars is viewed from the nightside. This is a result of finite gyro radius effects that are absent in the empirical and MHD models. Particles in the hybrid model follow cycloidal trajectories and are able to enter the field of view of the virtual instrument even though it is located in the "shadow" of the planet.

The hybrid model produces ENAs all the way down to the obstacle boundary, c. f., Fig. 7. In the MHD model on the other hand the production region is clearly separated from the planet. This is a result of the different grid resolutions. The smallest grid cell size is $R_m/20$ and $R_m/64$ for the hybrid and MHD models respectively.

The maximum of the hydrogen ENA production rate is located on the Mars-Sun line in the hybrid model, and away from the Mars-Sun line in the empirical and MHD models. In the MHD models there is a region of significant ENA production extending down to the Mars-Sun line, and the MHD model even shows two separated local maxima; one on the Mars-Sun line and one away from it. A few quantities resulting from the different models are compared in Table 3. For simplicity, the total hydrogen ENA production referred to in Table 3 was calculated by integrating the ENA production within a cylinder oriented along the x-axis from $x = -3R_m$ to $x = 3R_m$, and with a radius $\rho = 3R_m$. The exact shape of the integration volume is not important as long as all regions with high ENA-production are included. The solar wind hydrogen ENA flux corresponds to the local maximum in the direction of the Sun (at $\theta \approx 80°$) in the images with a solar zenith angle of 100°.

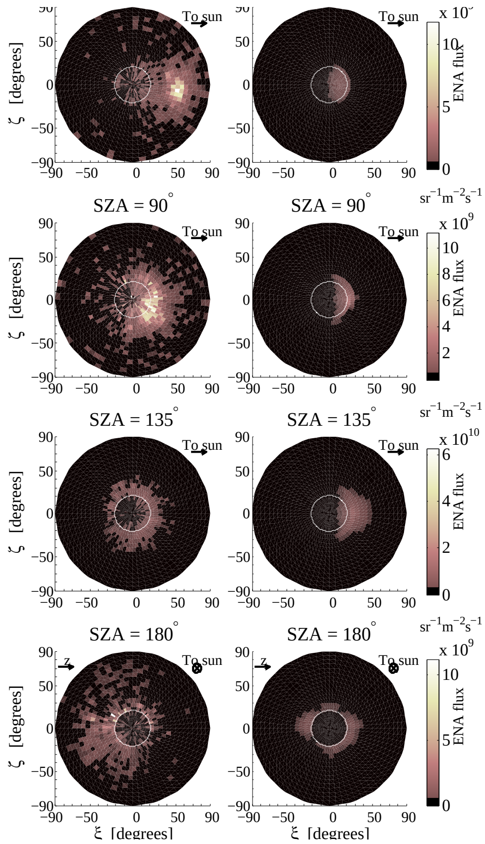

Fig. 15. Oxygen ENA images from the hybrid (left column) and MHD (right column) models. Panels that are on the same row show images from the same vantage point, i.e. a vantage point in the xz-plane ($z \geq 0$), $3R_m$ from the centre of Mars, and a solar zenith angles 45°, 90°, 135°, and 180°, starting from the top row. The colour scales are the same for panels on the same row.

Fig. 15 shows oxygen ENA images from the hybrid and MHD models, using the same colour scales for images from the same vantage point. The oxygen ENA images from the empirical model are not shown because the small amount of test particle data available produces images that are dominated by only a few pixels, and thus are less suitable for a comparison with other models using the same linear scale. This is a problem from which also the hybrid model is suffering making the images in the left hand column of Fig. 15 more spotty than the images from the MHD model shown in the right column.

In spite of the spottiness some differences between the two models can be pointed out. The oxygen ENA flux is clearly higher in the hybrid than in the MHD model. The emissions obtained in the MHD model are more concentrated to the interaction region close to the dayside of the planet, whereas the hybrid model produces more emissions that are spread out over a larger area. A possible explanation of this could be that since, in a single fluid MHD model the oxygen ions have to move in the direction of the mean plasma flow, we see oxygen emissions from roughly the same regions where we see hydrogen emissions; whereas in the hybrid model oxygen ions are treated as particles and are likely to follow more realistic trajectories, the oxygen gyro-radius being of the same order of magnitude as the radius of the planet. That the hybrid model does not include a realistic ionosphere may also be of importance.

In the bottom row of Fig. 15 it is seen that the asymmetry of the O^+ ion density distribution in the hybrid model also is detectable in the ENA images, and that there is no such asymmetry in the MHD model. The latter fact is more clearly seen in Fig. 13. This suggests that ENA images can serve as remote measurements of asymmetries in the O^+ density distribution. The ENA flux observed from the nightside is also much higher in the hybrid than in the MHD model, which could be a result of kinetic effects that are neglected in MHD.

The differences between the models regarding the O^+ density distribution and its possible dependence on the boundary conditions suggest that to make accurate predictions by the use of computer models, knowledge of the boundary conditions is required.

7 Discussion

What is the best way to model the interaction between the solar wind and the Martian atmosphere? Three different models have been investigated here. The empirical model provides us with a way to compare with the measurements while these are still quite scarce. However, when we wish to perform numerical experiments in order to understand the physics behind the observations we need to use self-consistent models.

What we really would like is a three-dimensional electromagnetic particle in cell simulation that treats both ions and electrons as particles, realistically includes the interaction with the neutral gas, and resolves phenomena on both the Debye length and the planetary radius scales. Such a model is unfortunately not possible to implement at this time with the limited computer resources available in the world today.

A requirement for the applicability of MHD is that the plasma must be collision dominated. This requirement is not at all met in the solar wind nor in the neighbourhood of Mars. The use of MHD has nevertheless turned out to be successful, since there are wave phenomena and turbulence “leading to a wide variety of wave particle interactions, which in turn act as pseudocollisions” (Ma et al., 2002) in thermalising the ion distribution functions. It would, of course, be desirable to take these phenomena properly into account rather than simply assuming that they exist and that they influence the plasma merely by providing thermalisation.

MHD completely neglects all finite gyro-radius effects, which is particularly troublesome when ions heavier than hydrogen are important. The oxygen ions in the Martian environment have gyro-radii comparable to the size of the planet. Their motion can hardly be predicted by MHD models, and thus such models are unlikely to be sufficient for the study of oxygen ENA images. For the protons, whose gyro-radius of about $0.3R_m$, the situation is slightly better, but far from being satisfactory. The absence of kinetic and finite gyro-radius effects is a limitation that is fundamental to MHD, and which will not improve with larger computer capacity. However, the presence of small scale plasma instabilities acting as pseudo-collisions may render MHD a good description of solar wind planetary interaction, even though kinetic and finite gyro-radius effects are not explicitly accounted for. Furthermore, in the magnetosheath where the magnetic field is stronger than in the solar wind, the gyro-radius is small, also for oxygen ions. Whether kinetic and finite gyro-radius effects make MHD insufficient remains to be seen when more observational data is obtained.

The hybrid model studied here, like MHD, suffers from the simplifying assumption of frozen-in field lines; in the hybrid model the magnetic field is frozen into the electron fluid, and in MHD it is frozen into the centre of mass frame, that is moving with the bulk velocity of the single fluid. This assumption is probably correct in the solar wind but may turn out to be wrong closer to Mars due to the finite conductivity. Furthermore, the results can be affected by the small number of super-particles per grid cell. It will be difficult to represent the full three-dimensional distribution function with only twenty particles, and that in a very large grid cell. The grid cell size is also a problem in the hybrid simulations, no small scale phenomena can possibly be resolved. If the grid cells were to be made smaller the number of particles would have to be increased in order to keep the number of particles per cell constant. The effects by the grid cell size and by the number of particles per cell can be lessened by an improved computer capacity.

This study also shows that not only the type of simulation code matters, but also the inclusion of relevant physical phenomena and boundary conditions. For example ionospheric emissions were included in the hybrid model but not the others. Another phenomenon that none of the models include is electron impact ionisation, which may be important (Zhang et al., 1993). Electron impact ionisation is also likely to be affected by acceleration of electrons by waves and magnetic field-aligned electric fields, that is, by processes that are neglected in both models. All models can be improved through the inclusion of more of the relevant physics and better knowledge of the boundary conditions.

Three different models that agree relatively well with the available observations, produce qualitatively different ENA images. This suggests that ENA imaging is a tool that is sensitive to kinetic and finite gyro radius effects, and to phenomena on both small and large scales.

8 Acknowledgments

This work was supported by the Swedish National Space Board.

References

Arkani-Hamed, J., 2001. A 50-degree spherical harmonic model of the magnetic field of Mars. Journal of Geophysical Research 106 (E10), 23197–23208.

Barabash, S., Holmström, M., Lukyanov, A., Kallio, E., 2002a. Energetic neutral atoms at Mars IV: Imaging of planetary oxygen. Journal of Geophysical Research 107 (A10), 1280, doi:10.1029/2001JA000326.

Barabash, S., Lundin, R., Andersson, H., et al., 2004b. ASPERA-3: Analyser of space plasmas and energetic ions for mars express. ESA Special PublicationSP-1240.

Chamberlain, J. W., Hunten, D. M., 1987. Theory of planetary atmospheres, 2nd Edition. Academic Press, inc., San Diego, California.

Gunell, H., Holmström, M., Biernat, H. K., Erkaev, N. V., 2004. Planetary ENA Imaging: Venus and a comparison with Mars, Accepted for publication in Planetary and Space Science.

Hodges, Jr., R. R., Breig, E. L., 1991. Ionosphere - exosphere coupling through charge exchange and momentum transfer in hydrogen-proton collisions. Journal of Geophysical Research 96 (A5), 7697–7708.

Holmström, M., Barabash, S., Kallio, E., 2002. Energetic neutral atoms at Mars I: Imaging of solar wind protons. Journal of Geophysical Research 107 (A10), 1277, doi:10.1029/2001JA000325.

Kallio, E., 1996. An empirical model of the solar wind flow around mars. Journal of Geophysical Research 101, 11133–11147.

Kallio, E., Janhunen, P., 2001. Atmospheric effects of proton precipitaion in the Martian atmosphere and its connection to the Mars-solar wind interaction. Journal of Geophysical Research 106, 5617–5634.

Kallio, E., Janhunen, P., 2002. Ion escape from Mars in a quasi-neutral hybrid model. Journal of Geophysical Research 107 (A3), 1035, doi: 10.1029/2001JA000090.

Kallio, E., Koskinen, H., 1999. A test particle simulation of the motion of oxygen ions and solar wid protons near Mars. J. Geophys. Res. 104, 557–579.

Kallio, E., Luhmann, J. G., Barabash, S., 1997. Charge exchange near Mars:

The solar wind absorption and energetic neutral atom production. Journal of Geophysical Research 102, 22183–22197.

Krasnopolsky, V. A., Gladstone, G. R., 1996. Helium on Mars: EUVE and PHOBOS data and implications for Mars' evolution. Journal of Geophysical Research 101 (A7), 15765–15772.

Ma, Y., Nagy, A. F., Hansen, K. C., DeZeeuw, D. L., Gombosi, T. I., 2002. Three-dimensional multispecies MHD studies of the solar wind interaction with Mars in the presence of crustal fields. Journal of Geophysical Research 107 (A10), 1282, doi:10.1029/2002JA009293.

Zhang, M. H. G., J. G. Luhmann, A. F. Nagy, J. R. Spreiter, and S. S. Stahara, Oxygen ionization rates at Mars and Venus: Relative contributions of impact ionization and charge exchange, Journal of Geophysical Research 98 (E2), 3311–3318, 1993.